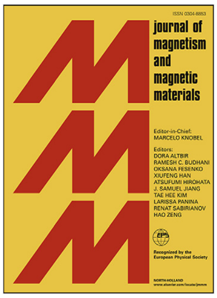

Finite element level validation of an anisotropic hysteresis model for non-oriented electrical steel sheets

Brijesh Upadhaya, Paavo Rasilo, Paul Handgruber, Anouar Belahcen, Antero Arkkio

PII: S0304-8853(22)00863-0
DOI: https://doi.org/10.1016/j.jmmm.2022.169978
Reference: MAGMA 169978

To appear in: *Journal of Magnetism and Magnetic Materials*

Received date : 24 May 2022
Revised date : 4 July 2022
Accepted date : 16 September 2022

Please cite this article as: B. Upadhaya, P. Rasilo, P. Handgruber et al., Finite element level validation of an anisotropic hysteresis model for non-oriented electrical steel sheets, *Journal of Magnetism and Magnetic Materials* (2022), doi: https://doi.org/10.1016/j.jmmm.2022.169978.

Finite Element Level Validation of an Anisotropic Hysteresis Model for Non-Oriented Electrical Steel Sheets

Brijesh Upadhaya

Department of Electrical Engineering and Automation, Aalto University, FI-00076 Espoo, Finland

Paavo Rasilo

Unit of Electrical Engineering, Tampere University, FI-33014 Tampere, Finland

Paul Handgruber

Institute of Fundamentals and Theory in Electrical Engineering, Graz University of Technology, A-8010 Graz, Austria

Anouar Belahcen

Department of Electrical Engineering and Automation, Aalto University, FI-00076 Espoo, Finland

Antero Arkkio

Department of Electrical Engineering and Automation, Aalto University, FI-00076 Espoo, Finland

---

Abstract

This paper presents the finite element level validation of the anisotropic Jiles-Atherton hysteresis model. Numerical analysis of a round rotational single sheet tester is performed using the 2D finite element method. Anisotropic extension of the Jiles-Atherton hysteresis model is coupled with the 2D finite element method. The finite element simulations are performed for the cases when the magnetic field alternates and rotates in the lamination plane. The simulated results for alternating and rotational flux density excitations agree with the measured data. The measured data used in this paper corresponds to the M400-50A nonoriented silicon steel.

Keywords:
Finite Element Analysis, Jiles-Atherton, Magnetic Anisotropy, Magnetic Hysteresis, Non-oriented Silicon Steel

---

Preprint submitted to Journal of Magnetism and Magnetic Materials *September 23, 2022*

1. Introduction

Nonoriented (NO) silicon steels are suitable for electromagnetic applications where the core experience directionally varying magnetic fields, for example, the stator yoke of a medium-sized induction motor [1]. The magnetic field can alternate and rotate in the stator core, depending on the location. A phenomenological hysteresis model should predict the magnetic fields for different types of excitations: alternating, rotating, and elliptical. The model should also describe magnetic responses under external stress and thermal loadings [2, 3, 4]. However, a physics-based hysteresis model of such caliber is unavailable [5].

The NO silicon steel possesses a significant level of magnetic anisotropy [6, 7, 8, 9]. Several models of magnetic anisotropy have been proposed for NO silicon steel. In [10], a method based on magnetic energy is proposed to account for magnetic anisotropy observed in the NO silicon steel. The model expresses energy with a Gumbel-type distribution, whose parameters are extracted utilizing the anhysteretic data. The model is suitable for the finite element method (FEM). However, the results they predict disagree with the measurement data. Instead of using the magnetic energy, [11] employs bicubic splines to represent the anhysteretic characteristics identified from the rotational measurements. The method based on the surface bicubic spline is easier to integrate with the FEM and it is more accurate than the energy-density method. Contrarily, [12] expresses magnetic energy using the Fourier series. The coefficients of the Fourier series-based model are identified using anhysteretic data in several measurement directions. [13] shows that the Fourier series-based anisotropic model is well adapted to the FEM by simulating the magnetic field in an interior permanent magnet machine composed of NO silicon steel.

Alternatively, [14] has modified Mayergoyz's approach to model anisotropy observed in a NO silicon steel sheet. The modification adds the Everett data from the alternating measurements in several directions. The anisotropic generalization of Mayergoyz's model controls the amplitude of the input projections, introducing anisotropy in the predicted results. [15] and [16] extend vector version of the Jiles-Atherton (JA) model to include magnetic anisotropy. Their extension considers measurement data in only two directions—the rolling and transverse. The anisotropic extension of the JA model estimates the field strength loci based on the parameters from rolling direction (RD) and transverse direction (TD) in the intermediate directions. Likewise, [17] and [18] implement anisotropy in the energy-based (EB) hysteresis model to predict variations in alternating and rotational field strength in a NO silicon steel sheet. The anisotropic EB model utilizes parameters identified from the alternating measurements in the RD and TD. Moreover, the pinning field probability density is represented by a univariate Gaussian-type distribution, whose parameters are estimated by fitting the model to the measurement data [17].

Likewise, [19] presents an anisotropic play-type model similar to [17]'s. The model considers parameters from the alternating measurements in all principal axes: the RD, TD, and the silicon steel lamination's thickness. The anisotropic play-type model shows a reasonably good fit for the magnetic field alternating in the RD, TD, and 45° directions. Moreover, [20] proposes an anisotropic play-type model. The model introduces anisotropy in the isotropic play-type model with the parameters identified from several unidirectional alternating measurements. The anisotropic play-type model yields a reasonably good fit with the measured data for NO silicon steel.

A physics-based multi-scale model (MSM) can be employed to predict the anisotropic behavior in a NO silicon steel lamination [21]. However, the MSM uses texture data, requiring complex measurements. Additionally, the MSM is a large minimization problem and computationally heavy. For the FEA, a simplified MSM is considered in [22]. The anhysteretic magnetization identified from the simplified MSM is fed to the hysteresis models—such as JA, EB, and Hauser [23, 24]. In [22], the simplified MSM-JA model is coupled with the FEM to study the effect of stress-induced anisotropy in a switched reluctance motor. Moreover, [25] couples the MSM with the EB model to account for the anisotropy observed in grain-oriented silicon steel. Nevertheless, the physics-based MSM-EB or MSM-JA model could be a good choice for predicting magnetic behavior in the NO silicon steel [22, 25].

Characterization of NO silicon steel is an essential part of the electrical machine design process [26]. An Epstein frame is a standardized device for measuring alternating BH characteristics. However, the Epstein frame is limited to alternating fields. A rotational single sheet tester is employed to measure rotational fields because it allows measurements of vector components using the field sensing methods [27]. A round rotational single sheet tester (RRSST) is a popular choice as it ensures better rotation of the flux density, utilizing a larger measuring region. Additionally, the RRSST allows measurement of alternating and rotational magnetic flux density—magnitudes as high as 2 T [28, 29].

This paper presents the finite element analysis (FEA) of an RRSST sample—a NO silicon steel disk of grade M400-50A. The FEA considers anisotropic and isotropic Jiles-Atherton (JA) hysteresis models [30]. The following four cases are considered for the FEA: flux density alternating in the RD, alternating in the 45° direction (ALT45), alternating in the TD, and rotating in the counter clock-wise direction (ROT). The anisotropic JA model (AJAM) utilizes the anhysteretic magnetization from alternating BH measurements in seven directions: 0°, 15°, 30°, . . . , 90° [30]. Moreover, the JA model's parameters vary as a function of the magnitude and polar direction of the flux density [31]. The unidirectional alternating BH measurements are used to estimate the JA model's parameters. In contrast, rotational measurements are used for validation (see Table 1).

Table 1: Magnetic measurements for the parameter identification and model validation.

Measurement type	Parameter identification	Model validation
RD	$\surd$	$\surd$
ALT45	-	$\surd$
TD	$\surd$	$\surd$
ROT	-	$\surd$

2. Methodology

2.1. Anisotropic JA Model

This paper considers AJAM explained in [30]—an improved extension of Bergqvist's vector JA model [32]. The model equations are re-summarized in the following:

Differential Susceptibility

Bergqvist's vector JA model defines differential susceptibility [15]:

$$\frac{\partial \boldsymbol{M}}{\partial \boldsymbol{H}} = \left[\mathbf{I} - (\boldsymbol{\chi}\alpha + c\boldsymbol{\xi}\alpha)\right]^{-1}\left[\boldsymbol{\chi} + c\boldsymbol{\xi}\right], \tag{1}$$

where $\mathbf{I}$ is the identity matrix, $\boldsymbol{\xi}$ and $\boldsymbol{\chi}$ are the differential anhysteretic and irreversible susceptibilities, $\alpha \geq 0$ is a parameter that represents interdomain coupling, and $c \in [0,1]$ is another parameter that quantifies the reversible processes associated with the bowing of domain walls ($c = 1$ corresponds to a completely reversible process) [33, 34]. The differential susceptibility in (1) is expressed using an auxiliary vector $\boldsymbol{\chi}_\mathrm{f} = \frac{1}{k}\left(\boldsymbol{M}_\mathrm{an} - \boldsymbol{M}\right)$ as follows:

$$\boldsymbol{\chi} = \begin{cases} \dfrac{\boldsymbol{\chi}_\mathrm{f}\boldsymbol{\chi}_\mathrm{f}^\mathsf{T}}{\|\boldsymbol{\chi}_\mathrm{f}\|} & \text{if } (\boldsymbol{M}_\mathrm{an} - \boldsymbol{M}) \cdot \partial \boldsymbol{H}_\mathrm{eff} > 0, \\ \mathbf{0} & \text{otherwise,} \end{cases} \tag{2}$$

where $k \geq 0$ is a parameter associated with the pinning of domain walls, $\boldsymbol{M}_\mathrm{an}$ represents the anhysteretic magnetization, and $\boldsymbol{H}_\mathrm{eff} = \boldsymbol{H} + \alpha\boldsymbol{M}$ is the effective field strength. The condition in (2) reflects the assumption that irreversible changes occur only when the field $\boldsymbol{H}_\mathrm{eff}$ is incremented in the direction of $(\boldsymbol{M}_\mathrm{an} - \boldsymbol{M})$.

Differential Reluctivity

The FEM based on magnetic vector potential formulation uses differential reluctivity [35]:

$$\frac{\partial \boldsymbol{H}}{\partial \boldsymbol{B}} = \left(\frac{\partial \boldsymbol{B}}{\partial \boldsymbol{H}}\right)^{-1} = \frac{1}{\mu_0}\left(\mathbf{I} + \frac{\partial \boldsymbol{M}}{\partial \boldsymbol{H}}\right)^{-1}, \tag{3}$$

where μ_0 is the permeability of the free space, $\dfrac{\partial \boldsymbol{B}}{\partial \boldsymbol{H}}$ represents the differential permeability, and $\dfrac{\partial \boldsymbol{M}}{\partial \boldsymbol{H}}$ is the differential susceptibility given by (1).

Anhysteretic Magnetization

The anhysteretic magnetization for the isotropic case is usually expressed as [35]

$$\boldsymbol{M}_{\mathrm{an}} = M_{\mathrm{an}} \frac{\boldsymbol{H}_{\mathrm{eff}}}{H_{\mathrm{eff}}}, \tag{4}$$

where $H_{\mathrm{eff}} = \|\boldsymbol{H}_{\mathrm{eff}}\|$ is the norm of effective field, and $M_{\mathrm{an}} = f\left(H_{\mathrm{eff}}\right)$ describes the anhysteretic curve identified from the unidirectional alternating BH loop. The differential anhysteretic susceptibility is expressed as

$$\boldsymbol{\xi} = \frac{M_{\mathrm{an}}}{H_{\mathrm{eff}}} \left[\mathbf{I} - \frac{\boldsymbol{H}_{\mathrm{eff}} \boldsymbol{H}_{\mathrm{eff}}^{\mathrm{T}}}{H_{\mathrm{eff}}^2} \right] + \frac{\partial M_{\mathrm{an}}}{\partial H_{\mathrm{eff}}} \frac{\boldsymbol{H}_{\mathrm{eff}} \boldsymbol{H}_{\mathrm{eff}}^{\mathrm{T}}}{H_{\mathrm{eff}}^2}. \tag{5}$$

In this paper, M_{an} defined in (4) is identified by averaging the unidirectional alternating BH characteristics measured in seven directions: 0°, 15°, 30°, . . . , 90°. Because the measurement is performed at an excitation frequency of 50 Hz, the hysteretic field strength is extracted by subtracting the eddy-current loss field from the measured field strength $\boldsymbol{H}_{\mathrm{meas}}$:

$$\boldsymbol{H} = \boldsymbol{H}_{\mathrm{meas}} - \sigma \frac{d^2}{12} \frac{\partial \boldsymbol{B}}{\partial t}, \tag{6}$$

where σ and d represent the electrical conductivity and thickness of the NO silicon steel sample. The derivative on the right-hand side of (6) is evaluated using the central difference method. After that, the phase shift between $\boldsymbol{H}$ and $\boldsymbol{B}$ is neglected, meaning $\boldsymbol{H}$ and $\boldsymbol{B}$ are projected in the reference direction, which is the polar direction of vector $\boldsymbol{B}$. This process is performed for all the measurement directions. The field strength is averaged because the measurement is B-controlled [31]:

$$H_{\mathrm{avg},i} = \frac{1}{7} \sum_{j=1}^{7} H_{\theta_j,i}, \tag{7}$$

where $\theta_j = (j-1)15°$ is the polar direction of $\boldsymbol{B}$, $i = 1, 2, 3, \ldots, N$ represents the data point index, and N is the total number of data points in one excitation cycle. Thus, M_{an} is obtained by averaging the ascending and descending brances of the major $B(H_{\mathrm{avg}})$-loop [36].

The anhysteretic magnetization follows a more generic expression for the anisotropic case:

$$\boldsymbol{M}_{\mathrm{an}} = M_{\mathrm{an,x}}(H_{\mathrm{eff}}, \vartheta)\boldsymbol{e}_{\mathrm{x}} + M_{\mathrm{an,y}}(H_{\mathrm{eff}}, \vartheta)\boldsymbol{e}_{\mathrm{y}}, \tag{8}$$

where ϑ is the polar angle of $\boldsymbol{H}_{\mathrm{eff}}$. The components of the anhysteretic magnetization (8) could be modeled using the multiscale approach [21]. However, the multiscale approach is a large minimization problem and computationally heavy. Analytical representation of the anhysteretic characteristic is possible with the help of transcendental functions [25]. Nevertheless, to ease the computational burden, this paper applies bicubic splines [30]. Explicitly, in each rectangle k,

$$M^{\mathrm{k}}_{\mathrm{an,x}}(H_{\mathrm{eff}}, \vartheta) = \begin{bmatrix}1 & H_{\mathrm{eff}} & H^2_{\mathrm{eff}} & H^3_{\mathrm{eff}}\end{bmatrix} \boldsymbol{\beta}^{\mathrm{k}}_{\mathrm{x}} \begin{bmatrix}1 & \vartheta & \vartheta^2 & \vartheta^3\end{bmatrix}^{\mathtt{T}}, \tag{9}$$

$$M^{\mathrm{k}}_{\mathrm{an,y}}(H_{\mathrm{eff}}, \vartheta) = \begin{bmatrix}1 & H_{\mathrm{eff}} & H^2_{\mathrm{eff}} & H^3_{\mathrm{eff}}\end{bmatrix} \boldsymbol{\beta}^{\mathrm{k}}_{\mathrm{y}} \begin{bmatrix}1 & \vartheta & \vartheta^2 & \vartheta^3\end{bmatrix}^{\mathtt{T}}, \tag{10}$$

where $\boldsymbol{\beta}^{\mathrm{k}}_{\mathrm{x}}$ and $\boldsymbol{\beta}^{\mathrm{k}}_{\mathrm{y}}$ are 4×4 coefficient matrices whose elements are identified from the anhysteretic M(H) characteristics (see [30, Fig. 2]). The source code available in [37] is used to obtain the elements of $\boldsymbol{\beta}^{\mathrm{k}}_{\mathrm{x}}$ and $\boldsymbol{\beta}^{\mathrm{k}}_{\mathrm{y}}$. The elements of $\boldsymbol{\xi}$ are evaluated from (9) and (10) using the following polar-to-Cartesian transformation:

$$\boldsymbol{\xi} = \begin{bmatrix} \dfrac{\partial M_{\mathrm{an,x}}}{\partial H_{\mathrm{eff,x}}} & \dfrac{\partial M_{\mathrm{an,x}}}{\partial H_{\mathrm{eff,y}}} \\ \dfrac{\partial M_{\mathrm{an,y}}}{\partial H_{\mathrm{eff,x}}} & \dfrac{\partial M_{\mathrm{an,y}}}{\partial H_{\mathrm{eff,y}}} \end{bmatrix} = \begin{bmatrix} \dfrac{\partial M_{\mathrm{an,x}}}{\partial H_{\mathrm{eff}}} & \dfrac{\partial M_{\mathrm{an,x}}}{\partial \vartheta} \\ \dfrac{\partial M_{\mathrm{an,y}}}{\partial H_{\mathrm{eff}}} & \dfrac{\partial M_{\mathrm{an,y}}}{\partial \vartheta} \end{bmatrix} \begin{bmatrix} \cos\vartheta & \sin\vartheta \\ -\dfrac{\sin\vartheta}{H_{\mathrm{eff}}} & \dfrac{\cos\vartheta}{H_{\mathrm{eff}}} \end{bmatrix}. \tag{11}$$

Directional Variation of JA Parameters

The following equations describe the directional variations of the JA model's parameters [31]:

$$X_{\mathrm{JA}}(B, \theta) = \frac{P_{\mathrm{x}}(B)\, P_{\mathrm{y}}(B)}{\sqrt{(P_{\mathrm{x}}(B)\sin\theta)^2 + (P_{\mathrm{y}}(B)\cos\theta)^2}}, \tag{12}$$

where $X_{\mathrm{JA}} = \{k, \alpha, c\}$, $P_{\mathrm{x}} = \{k_{\mathrm{x}}, \alpha_{\mathrm{x}}, c_{\mathrm{x}}\}$, $P_{\mathrm{y}} = \{k_{\mathrm{y}}, \alpha_{\mathrm{y}}, c_{\mathrm{y}}\}$, and B and θ represent the norm and polar direction of $\boldsymbol{B}$. The parameters are identified from the unidirectional alternating BH measurements in only two directions—the RD and TD. The parameters in the right hand side of (12) are represented with a piecewise linear polynomial along the magnitude of the flux density (see [30, Fig. 5]).

2.2. Finite Element Modeling

This section considers a magnetostatic field problem in a domain $\Omega \in \mathbb{R}^2$. The domain is a collection of linear Ω_{L} and nonlinear Ω_{N} subdomains: $\Omega = \Omega_{\mathrm{L}} + \Omega_{\mathrm{N}}$.

The spatial variation of the magnetic field strength in Ω is described by the following partial differential equation:

$$\nabla \times \boldsymbol{H} = \boldsymbol{J}_{\mathrm{s}}, \tag{13}$$

where $\boldsymbol{J}_{\mathrm{s}} = J(x, y)\boldsymbol{e}_{\mathrm{z}}$ is the source current density—usually imposed on the subdomain Ω_{L}. A hysteretic material law $\boldsymbol{H} = \mathscr{H}(\boldsymbol{B})$ links $\boldsymbol{H}$ and $\boldsymbol{B}$ in Ω_{N}, whereas, in Ω_{L}, a linear relationship $\boldsymbol{H} = \nu_0\boldsymbol{B}$, where $\nu_0 = 1/\mu_0$, exists between them.

For any continuous vector potential $\boldsymbol{A} = A(x, y)\boldsymbol{e}_{\mathrm{z}}$, the flux density $\boldsymbol{B} = \nabla \times \boldsymbol{A}$, and $\boldsymbol{A}$ satisfies the Coloumb gauge, $\nabla \cdot \boldsymbol{A} = 0$. The Galerkin method is employed to solve (13). The equation is multiplied by a weight function: $\boldsymbol{\phi} = \phi\boldsymbol{e}_{\mathrm{z}}$, and integrated over the domain Ω, resulting in [38]

$$(\mathscr{H}(\nabla \times \boldsymbol{A}), \nabla \times \boldsymbol{\phi})_{\Omega_{\mathrm{N}}} + (\nu_0\nabla \times \boldsymbol{A}, \nabla \times \boldsymbol{\phi})_{\Omega_{\mathrm{L}}} = (\boldsymbol{J}_{\mathrm{s}}, \boldsymbol{\phi})_{\Omega} - \langle \boldsymbol{H} \times \boldsymbol{n}, \boldsymbol{\phi}\rangle_{\Gamma}, \tag{14}$$

where $(\boldsymbol{u}, \boldsymbol{v})_{\Omega}$ and $\langle \boldsymbol{u}, \boldsymbol{v}\rangle_{\Gamma}$ denote the integration $\int_{\Omega}(\boldsymbol{u} \cdot \boldsymbol{v})\mathrm{d}\Omega$ and $\oint_{\Gamma}(\boldsymbol{u} \cdot \boldsymbol{v})\mathrm{d}\Gamma$, and $\boldsymbol{n}$ is the outward oriented unit vector normal to the boundary Γ of Ω. For simplicity, the contour integral on the right hand side of (14) is ommited. The boundary conditions will be discussed in a separate section.

Solution of the Nonlinear Field Equation by Fixed Point Method

The following constitutive relation is used to solve (14) by the fixed-point method [39, 40]

$$\mathscr{H}(\nabla \times \boldsymbol{A}) = \nu_{\mathrm{FP}}\nabla \times \boldsymbol{A} + \boldsymbol{R}, \tag{15}$$

where ν_{FP} is a reluctivity like quantity, and $\boldsymbol{R}$ is a magnetization like quantity. Thus, using (3),

$$\nu_{\mathrm{FP}} = \frac{\partial H_{\mathrm{x}}}{\partial B_{\mathrm{x}}} + \frac{\partial H_{\mathrm{y}}}{\partial B_{\mathrm{y}}}. \tag{16}$$

Moreover, using (15) in (14) results in the linearized system:

$$(\nu_{\mathrm{FP}}\nabla \times \boldsymbol{A}, \nabla \times \boldsymbol{\phi})_{\Omega_{\mathrm{N}}} + (\nu_0\nabla \times \boldsymbol{A}, \nabla \times \boldsymbol{\phi})_{\Omega_{\mathrm{L}}} = (\boldsymbol{J}_{\mathrm{s}}, \boldsymbol{\phi})_{\Omega} - (\boldsymbol{R}, \nabla \times \boldsymbol{\phi})_{\Omega_{\mathrm{N}}}. \tag{17}$$

In the FEM, the approximation of the vector potential

$$\boldsymbol{A} = \sum_{i=1}^{N} a_i\varphi_i(x, y)\boldsymbol{e}_{\mathrm{z}}, \tag{18}$$

where a_i and φ_i are the nodal value and shape function associated with node i of the finite element (FE) mesh, and N represents the total number of nodes. Commonly, the shape functions connected to the free nodes are used as the weight functions. This paper adopts the triangular elements to discretize Ω, utilizing linear shape functions so that the weight functions are linear basis functions [38].

Equation (17) is expressed in the following form:

$$(\boldsymbol{K}_\mathrm{N} + \boldsymbol{K}_\mathrm{L})\,\boldsymbol{a} = \boldsymbol{C}J - \boldsymbol{D}\boldsymbol{R}, \tag{19}$$

where $\boldsymbol{a} = [a_1, \ldots, a_N]^\mathsf{T}$ is the vector of nodal values, $[\boldsymbol{K}_\mathrm{N}]_{i,j} = (\nu_\mathrm{FP}\nabla\phi_i, \nabla\phi_j)$ and $[\boldsymbol{K}_\mathrm{L}]_{i,j} = (\nu_0\nabla\phi_i, \nabla\phi_j)$ are the linear parts of the stiffness matrix, $[\boldsymbol{C}]_j = (\cdot, \phi_j)$ is a vector connecting the source current density $\boldsymbol{J}$, and $[\boldsymbol{D}]_{i,j} = \left([\partial_\mathrm{y}\phi_i \;\; -\partial_\mathrm{x}\phi_j]^\mathsf{T}, \cdot\right)$ matrix links the nonlinear residual $\boldsymbol{R} = [R_\mathrm{x}\; R_\mathrm{y}]^\mathsf{T}$.

More generally, (19) can be formally written as follows:

$$\boldsymbol{S}\boldsymbol{a}_{k+1}^{n+1} = \boldsymbol{f}_{k+1}^{n}, \tag{20}$$

where $\boldsymbol{S} = \boldsymbol{K}_\mathrm{N} + \boldsymbol{K}_\mathrm{L}$ is the system matrix, which is usually sparse and symmetric, and $\boldsymbol{f}_{k+1}^{n} = \boldsymbol{C}J_{k+1} - \boldsymbol{D}\boldsymbol{R}_{k+1}^{n}$ is the load vector, subscripts $k+1$ and k denote the current and previous time instant, and superscripts $n+1$ and n denote the current and previous iterate. This paper uses the sparse direct linear solver to solve the system of linear equations (20) [41]. The nonlinear iterations in (20) are stopped if the L^1 norm of the change in solution ensures

$$|a_{k+1}^{n+1} - a_{k+1}^{n}| < \epsilon_\mathrm{abs} + \epsilon_\mathrm{rel}|a_{k+1}^{n}| \quad \text{and} \quad n_\mathrm{min} < n \leq n_\mathrm{max}, \tag{21}$$

where ϵ_abs and ϵ_rel represent the absolute and relative tolerances, and n_min and n_max denote the minimum and maximum nonlinear iterations.

Boundary Condition

The following boundary condition is applied on the outer boundary of the RRSST sample to set the magnetic flux density to alternate in any arbitrary direction θ:

$$A_\mathrm{b} = \hat{A}_\mathrm{b}\sin(\vartheta - \theta)\sin(\omega t), \tag{22}$$

where A_b is the z-component of the vector potential on the outer boundary Γ, $\hat{A}_\mathrm{b}$ is the peak amplitude of the vector potential, ϑ is the angular coordinate of the particular point on the boundary, $\omega = 2\pi f$ is the angular frequency, and f is the frequency in cycles per second.

Moreover, the flux density rotates on the sample if the vector potential satisfies the following condition [42]:

$$A_\mathrm{b} = \hat{A}_\mathrm{b}\sin(\vartheta - \omega t)\,. \tag{23}$$

The flux density's amplitude $\hat{B}$ is controlled by controlling the value of $\hat{A}_\mathrm{b}$. Thus, using $\hat{A}_\mathrm{b} = r\hat{B}$, where r is the radius of the circular steel sheet, in (22) and (23), respectively. Furthermore, considering the Dirichlet boundary condition, (20) is expressed as follows:

$$\begin{bmatrix} \boldsymbol{S}_\mathrm{hh} & \boldsymbol{0} \\ \boldsymbol{0} & \mathbf{I} \end{bmatrix} \begin{bmatrix} \boldsymbol{a}_{\mathrm{h},k+1}^{n+1} \\ \boldsymbol{a}_{\mathrm{b},k+1}^{n+1} \end{bmatrix} = -\begin{bmatrix} \boldsymbol{S}_\mathrm{hh} & \boldsymbol{S}_\mathrm{hb} \\ \boldsymbol{0} & \boldsymbol{0} \end{bmatrix} \begin{bmatrix} \boldsymbol{0} \\ \boldsymbol{a}_{\mathrm{b},k+1}^{n+1} \end{bmatrix} + \begin{bmatrix} \boldsymbol{f}_{\mathrm{h},k+1}^{n} \\ \boldsymbol{f}_{\mathrm{b},k+1}^{n} \end{bmatrix}, \tag{24}$$

where the additional subscripts h and b denote the free and fixed boundary nodes.

FE mesh of the RRSST

The layout of the RRSST is detailed in [30, Fig. 4]. Fig. 1 is the 2D FE mesh of the circular steel sample. The mesh is generated using the freely available meshing software Gmsh [43]. The mesh consists of two material domains: air and silicon steel. The elements with yellow edges represent the air domain, whereas those with red and blue edges represent silicon steel. The elements with blue edges distinguish the sensor region from the remaining core. The mesh consists of 29682 elements, of which 144 are air elements, and the remaining 29538 elements represent silicon steel core. There are 14898 nodes, of which 112 belong to the outer boundary, and the remaining 14786 are internal free nodes.

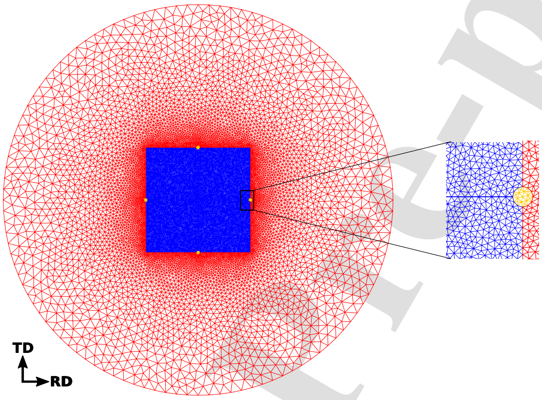

Figure 1: 2D FE mesh of the RRSST sample. The sensor region includes four holes that are drilled to accommodate the B-coils. The radius of the circular steel sample $r = 39$ mm, and the hole $r_{\mathrm{hole}} = 0.4$ mm (see [30, Fig. 4]). A zoomed section on the right hand side depicts the triangular mesh inside the hole that is aligned in the RD.

Estimation of $\boldsymbol{B}$ and $\boldsymbol{H}$

The magnetic flux density in the sensor region (see Fig. 1) is obtained by using the following expression:

$$\boldsymbol{B} = \frac{\bar{A}_1 - \bar{A}_2}{l_{\mathrm{w}}}\boldsymbol{e}_{\mathrm{x}} + \frac{\bar{A}_3 - \bar{A}_4}{l_{\mathrm{w}}}\boldsymbol{e}_{\mathrm{y}}, \tag{25}$$

where

$$\bar{A}_i = \frac{1}{S_i}\int_{S_i} A\mathrm{d}S, \quad i = 1, 2, 3, 4,$$

denotes the average value of the z-component of the vector potential, S_i is the cross-sectional area of the i^{th} hole, and l_{w} is center-to-center distance between holes aligned in the RD or TD. Note that the holes with index $i = 1$ and 2 are aligned in the TD, and holes with index $i = 3$ and 4 are aligned in the RD. Likewise, the components of the magnetic field strength sensed by the H-coils, which is placed on the surface of the sample, are considered to be the weighted average:

$$\boldsymbol{H} = \left(\frac{1}{S}\int_S H_{\mathrm{x}}\mathrm{d}S\right)\boldsymbol{e}_{\mathrm{x}} + \left(\frac{1}{S}\int_S H_{\mathrm{y}}\mathrm{d}S\right)\boldsymbol{e}_{\mathrm{y}}, \tag{26}$$

where S is the total surface area of the sensor region excluding the holes.

Moreover, after estimating $\boldsymbol{B}$ and $\boldsymbol{H}$ from (25) and (26), the hysteresis loss density is evaluated using the following integral [44]:

$$w = \frac{1}{T}\int_0^T \left(\boldsymbol{H}\cdot\frac{\partial \boldsymbol{B}}{\partial t}\right)\mathrm{d}t. \tag{27}$$

The integral in the right hand side of (27) is numerically evaluated using the trapezoidal rule.

Evaluation of JA Parameters at Gauss Integration Points

The surface integral in the 2D FEM is obtained using the Gauss-Legendre quadrature rule [38]. The surface integration is converted to a weighted sum according to the quadrature rule. The parameters of the JA model are evaluated from the flux densities at the two previous steps at the integration point (IP):

$$X_{\mathrm{JA},\ell+1} = f\left(\max\{\|\boldsymbol{B}_\ell\|,\, \|\boldsymbol{B}_{\ell-1}\|\},\, \theta_{\boldsymbol{B}_\ell}\right), \tag{28}$$

where $X_{\mathrm{JA}} = \{k,\, c,\, \alpha\}$, and subscript ℓ denotes the time step. This paper considers only one IP—the centroid of the reference triangle.

2.3. The R-squared measure of goodness of fit

The R-squared (R^2) is used as a quantitative measure of goodness of fit between the predicted and measured magnetic data. The following equation defines the R^2:

$$R^2 = 1 - \frac{\sum_{i=1}^{N}(Y_{\mathrm{meas},i} - Y_{\mathrm{simu},i})^2}{\sum_{i=1}^{N}(Y_{\mathrm{meas},i} - \bar{Y}_{\mathrm{meas}})^2} \tag{29}$$

where Y_{meas} and Y_{simu} denote the measured and predicted values, $\bar{Y}$ is the mean value, and N denotes the total number of data points. For the RRSST, the goodness of fit is evaluated by setting $Y = \{B_{\mathrm{x}}, H_{\mathrm{x}}, B_{\mathrm{y}}, H_{\mathrm{y}}\}$ in (29). For an exact match between the predicted and measured results, $R^2 = 1$. Thus, a positive value of R^2 close to 1 could be considered a good fit.

3. Results and Discussion

This section presents the results of the 2D FEA of the RRSST sample. Equations (22) and (23) are considered to establish either unidirectionally alternating or rotating magnetic flux density in the circular steel sample. The magnitude of $\boldsymbol{B}$ is controlled by setting $\hat{B} = \{0.5, 1, 1.5\}$ T and $f = 1$ Hz in the equations describing the essential boundary conditions. The FE simulations are performed for the first five periods of the supply frequency. A single period of the supply frequency is discretized into 400 steps. The number of minimum allowed nonlinear iteration is set to be $n_{\text{min}} = 2$. The values of tolerances are fixed as $\epsilon_{\text{abs}} = 10^{-5}$ and $\epsilon_{\text{rel}} = 10^{-7}$. Equations (25) and (26) are used to estimate $\boldsymbol{B}$ and $\boldsymbol{H}$ in the sensor region of the RRSST sample. The last or fifth period of the magnetic field solution is considered to obtain the hysteresis loss density. The results of the FE simulations are in Figs. 2 - 10. The following subsections discuss the results.

3.1. $\boldsymbol{B}$ *alternating in the RD*

Fig. 2 shows the result when the magnetic flux density alternates parallel to the RD. The isotropic JA model (IJAM) considers BH characteristics averaged over seven directions, meaning the prediction would be closer to the magnetic characteristics in the 45° direction. Because the field strength is higher for the isotropic case, the losses would also be higher for the isotropic case than anisotropic. Fig. 3 compares the measured and simulated alternating BH characteristics in the RD. The results of the AJAM agree with the measured data. However, some differences are seen in the results of the IJAM. Clearly, the IJAM underestimates the BH characteristics when the flux density alternates in the RD.

3.2. $\boldsymbol{B}$ *alternating in the* 45° *direction*

Fig. 4 shows the result when the magnetic flux density alternates in the 45° direction. The differences between the results are difficult to see from the field distribution. The hysteresis loss distribution shows noticeable differences. The losses are higher for the AJAM than for the IJAM. Fig. 5 compares the measured and simulated BH loci. The BH characteristics predicted by the AJAM agree better with the measurement data than the IJAM. However, notable differences are seen at a high magnitude of the flux density.

3.3. $\boldsymbol{B}$ *alternating in the TD*

Fig. 6 shows the result when the magnetic flux density alternates in the TD. Because the TD is a hard direction of magnetization, the magnetic field strength is higher for the AJAM than IJAM. Consequently, the losses are higher for the anisotropic case. Fig. 7 compares the measured and simulated alternating BH

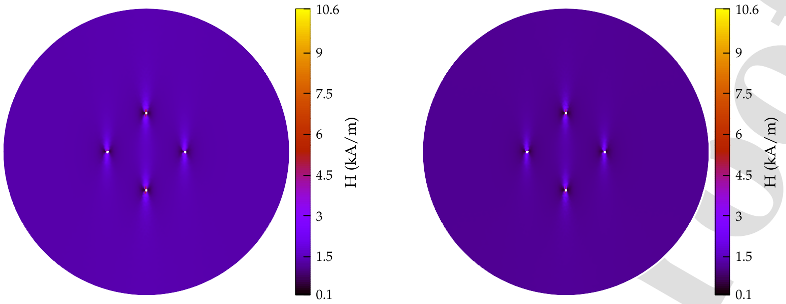

(a) IJAM's H (b) AJAM's H

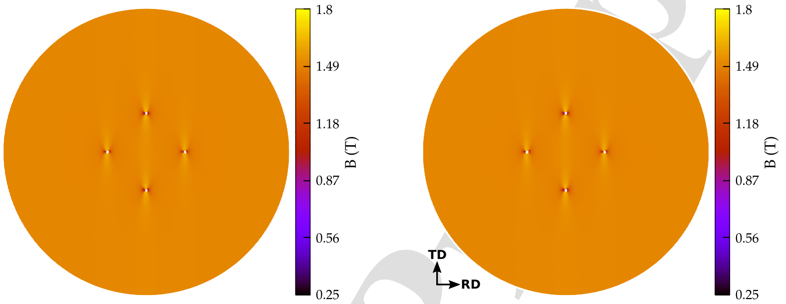

(c) IJAM's B (d) AJAM's B

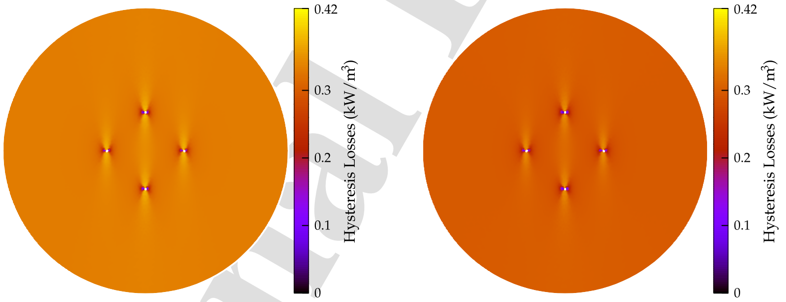

(e) IJAM's Losses (f) AJAM's Losses

Figure 2: Distribution of the magnetic field strength and flux density at a time instant $t = 4.25$ s, and time-averaged hysteresis losses in the RRSST sample. The magnetic flux density alternates in the RD. (a), (c) and (e) FEM coupled with the IJAM. (b), (d) and (f) FEM coupled with the AJAM.

characteristics. The AJAM's results are in good agreement with the measured data. In contrast, the IJAM's results differ significantly from the measured data.

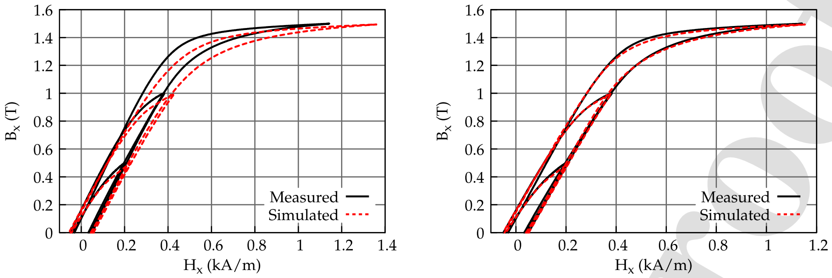

(a) IJAM (b) AJAM

Figure 3: Measured and FE simulated BH loops captured in the sensor region of the RRSST sample. The magnetic flux density alternates in the RD. (a) FEM coupled with the IJAM. (b) FEM coupled with the AJAM.

Thus, the IJAM underestimates the BH characteristics if the flux density alternates in the TD.

3.4. ***B*** *rotating in the counter-clockwise direction*

Fig. 8 shows the result when the magnetic flux density rotates in the counter clock-wise direction. The field quantities rotates at each step, so, it may not be intuitive to compare the results from two different models at a single time instant. Nevertheless, the hysteresis losses are evaluated from a full cycle of the input excitation, so, comparing the isotropic and anisotropic models is more intuitive. The distribution of the hysteresis loss density is more pronounced for the AJAM than IJAM (see Fig. 8a and Fig. 8b). The presence of easy and hard magnetization directions leads to different amounts of losses in different directions around the perimeter of the holes. The rest of the sample experiences uniform loss density distribution.

Fig. 9 compares the $H_{\mathrm{x}}(H_{\mathrm{y}})$, $B_{\mathrm{x}}(B_{\mathrm{y}})$, $B_{\mathrm{x}}(H_{\mathrm{x}})$, and $B_{\mathrm{y}}(H_{\mathrm{y}})$ characteristics. The results predicted by the AJAM agree with the measured data. However, notable differences are seen between the measured and simulated data at a high magnitude level. Conversely, the IJAM's prediction differs significantly from the measured data. Figs. 9e - 9h compare the measured $B_{\mathrm{x}}(H_{\mathrm{x}})$ and $B_{\mathrm{y}}(H_{\mathrm{y}})$ characteristics. The results of the AJAM agree with the measured data until 1 T. However, the differences are significant at 1.5 T. Contrarily, the IJAM's results differs considerably from the measured data.

3.5. Comparison of R-squared coefficient

Tables 2 and 3 show the R^2 values for the FEA results of the IJAM and AJAM. Note that the R^2 values are tabulated for the components of $\boldsymbol{H}$. For the

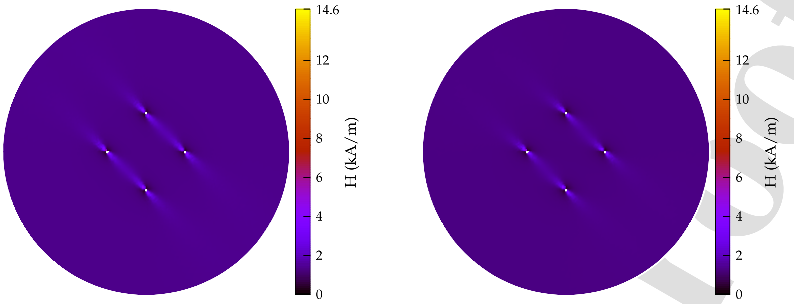

(a) IJAM's H (b) AJAM's H

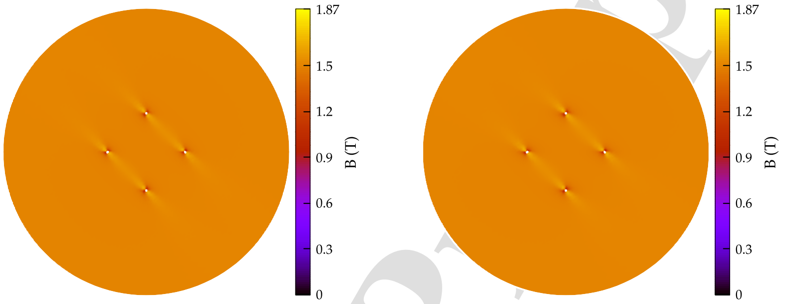

(c) IJAM's B (d) AJAM's B

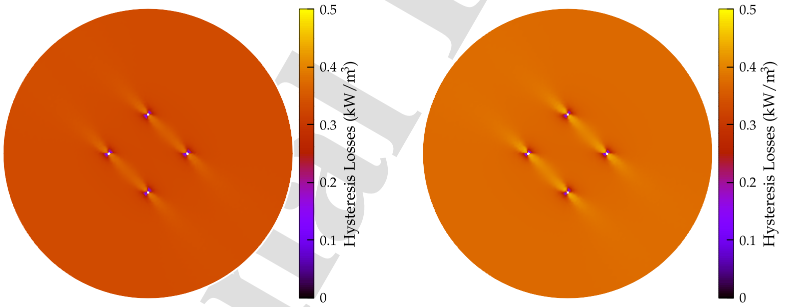

(e) IJAM's Losses (f) AJAM's Losses

Figure 4: Distribution of the magnetic field strength and flux density at a time instant $t = 4.25$ s, and time-averaged hysteresis losses in the RRSST sample. The magnetic flux density alternates in the 45° direction. (a), (c) and (e) FEM coupled with the IJAM. (b), (d) and (f) FEM coupled with the AJAM.

components of $\boldsymbol{B}$, $R^2 = 0.9999$ in all cases, so it is not tabulated. The R^2 values for the AJAM are higher than those for the IJAM, meaning the predictions

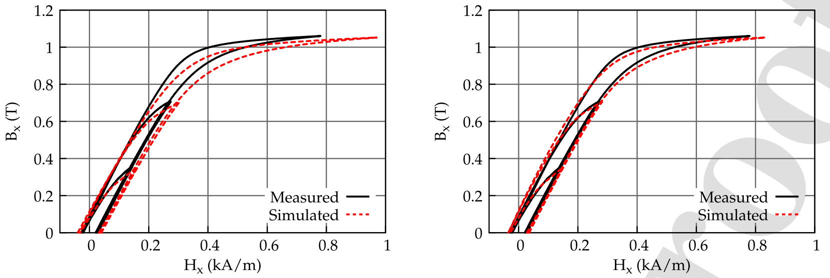

(a) IJAM (b) AJAM

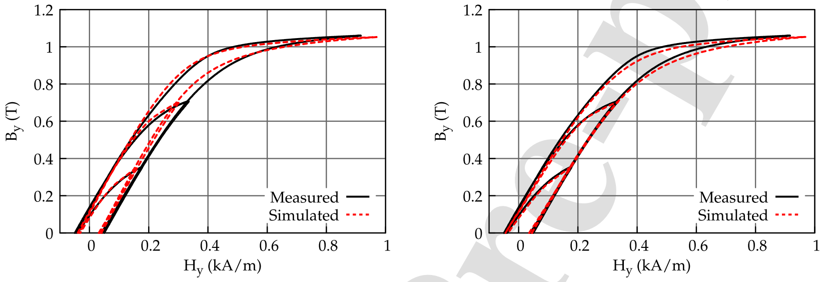

(c) IJAM (d) AJAM

Figure 5: Measured and FE simulated $B_{\mathrm{x}}(H_{\mathrm{x}})$ and $B_{\mathrm{y}}(H_{\mathrm{y}})$ loci obtained from the sensor region of the RRSST sample. The magnetic flux density alternates in the 45° direction. (a) and (c) FEM coupled with the IJAM. (b) and (d) FEM coupled with the AJAM.

are better for the AJAM. The R^2 values for IJAM decrease with an increase in excitation magnitude, signifying the predictions worsen at high flux density excitations.

Table 2: R^2 values for IJAM's predictions.

RRSST	$B = 0.5$ T		$B = 1.0$ T		$B = 1.5$ T	
excitation	H_{x}	H_{y}	H_{x}	H_{y}	H_{x}	H_{y}
RD	0.9861	–	0.9854	–	0.9678	–
ALT45	0.9820	0.9909	0.9879	0.9929	0.9557	0.9967
TD	–	0.9924	–	0.9883	–	0.9532
ROT	0.9881	0.9861	0.9767	0.9878	0.8693	0.9714

3.6. Comparison of hysteresis losses

Fig. 10 compares the hysteresis losses for four different types of input excitations. The IJAM should yield identical magnetic characteristics for alternating

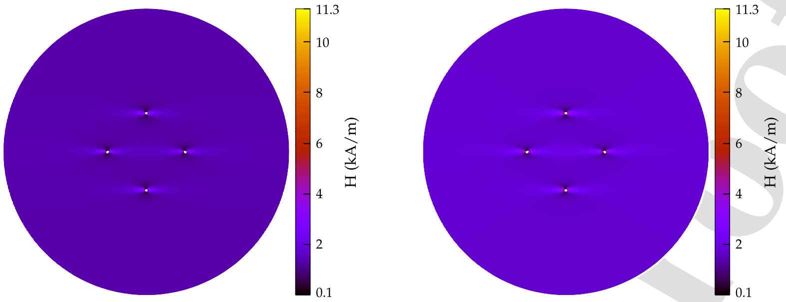

(a) IJAM's H (b) AJAM's H

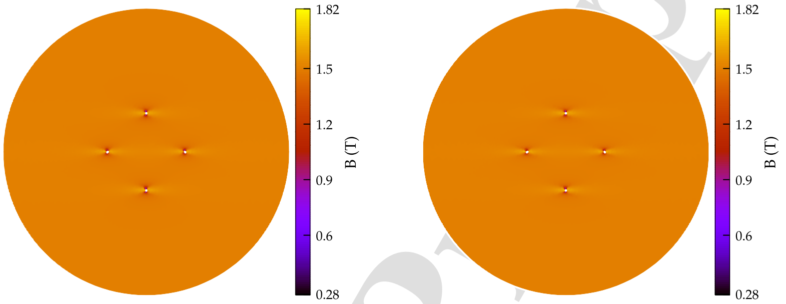

(c) IJAM's B (d) AJAM's B

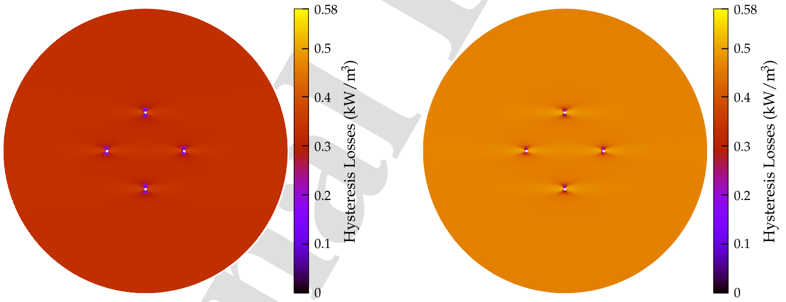

(e) IJAM's Losses (f) AJAM's Losses

Figure 6: Distribution of the magnetic field strength and flux density at time instant $t = 4.25$ s, and time-avaraged hysteresis losses in the RRSST sample. The magnetic flux density alternates in the TD. (a), (c) and (e) FEM coupled with the IJAM. (b), (d) and (f) FEM coupled with the AJAM.

input excitations, which means the losses should also be the same. Thus, according to the result presented in Fig. 10a, input excitations along RD, ALT45, and

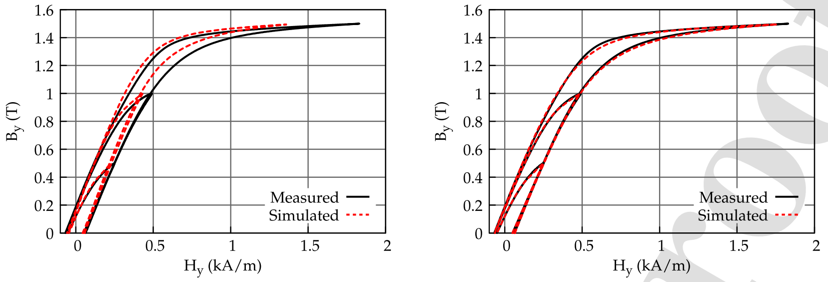

(a) IJAM (b) AJAM

Figure 7: Measured and FE simulated BH loops captured within the sensor region of the RRSST. The magnetic flux density alternates in the TD. (a) FEM coupled with the IJAM. (b) FEM coupled with the AJAM.

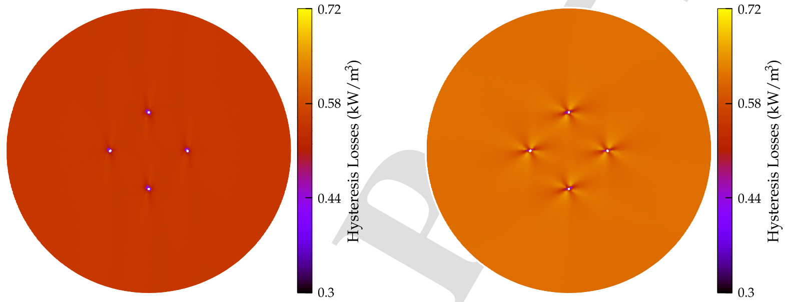

(a) IJAM's Losses (b) AJAM's Losses

Figure 8: Distribution of the magnetic field strength at flux density at time instant $t = 4.25$ s, and time-averaged hysteresis losses in the RRSST sample. The magnetic flux density is rotating counter clock-wise in the RRSST sample. (a), (c) and (e) represent FEM coupled with the IJAM. (b), (d) and (f) represent FEM coupled with the AJAM.

Table 3: R^2 values for AJAM's predictions.

RRSST excitation	$B = 0.5$ T		$B = 1.0$ T		$B = 1.5$ T	
	H_x	H_y	H_x	H_y	H_x	H_y
RD	0.9979	–	0.9999	–	0.9995	–
ALT45	0.9959	0.9986	0.9983	0.9993	0.9949	0.9963
TD	–	0.9996	–	0.9998	–	0.9990
ROT	0.9940	0.9966	0.9964	0.9997	0.9835	0.9847

TD yield similar losses. In contrast, for the anisotropic model, alternating losses depend on the direction of the input excitation. As shown in Fig. 10b, losses produced by the field alternating in the RD is the lowest, followed by ALT45 and TD. If we now compare rotational losses, we see that the differences are negligible until 1 T, and at 1.5 T, the AJAM yields higher losses in the RRSST sample.

3.7. Simulation time and iterations

The FE simulations are performed using Intel® Core™ M-5Y51 @1.10 GHz RAM 8GB with GNU/Linux environment. An in-house program written in the C programming language is used for the simulations. The information related to the simulation time and average number of nonlinear iterations are in Tables 4 and 5. The FE simulation that considers the IJAM spends about one second per step on average, whereas, the simulation times are on average 10% higher for the AJAM. Nevertheless, the average numbers of nonlinear iterations are the same.

Table 4: FE simulation time and nonlinear iterations for the IJAM.

RRSST excitation	CPU time and average number of iterations per step		
	$B = 0.5$ T	$B = 1.0$ T	$B = 1.5$ T
RD	1.02 s (3)	0.98 s (3)	0.99 s (3)
ALT45	0.99 s (3)	1.00 s (3)	0.99 s (3)
TD	0.99 s (3)	0.98 s (3)	1.03 s (3)
ROT	0.99 s (3)	0.99 s (3)	0.99 s (3)

Table 5: FE simulation time and nonlinear iterations for the AJAM.

RRSST excitation	CPU time and average number of iterations per step		
	$B = 0.5$ T	$B = 1.0$ T	$B = 1.5$ T
RD	1.11 s (3)	1.12 s (3)	1.13 s (3)
ALT45	1.12 s (3)	1.13 s (3)	1.13 s (3)
TD	1.11 s (3)	1.13 s (3)	1.10 s (3)
ROT	1.11 s (3)	1.13 s (3)	1.13 s (3)

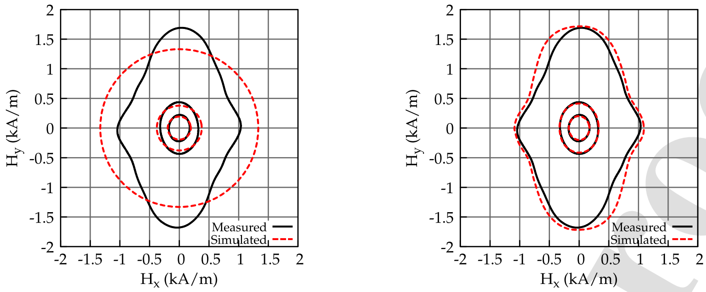

(a) IJAM (b) AJAM

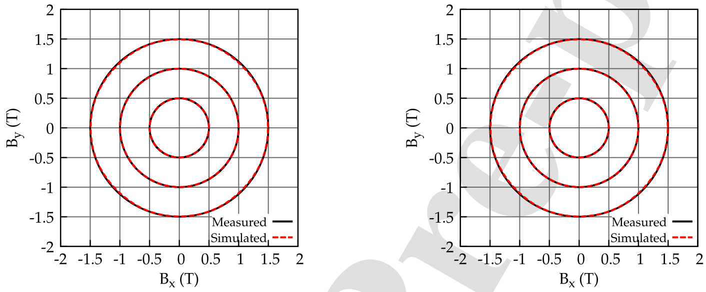

(c) IJAM (d) AJAM

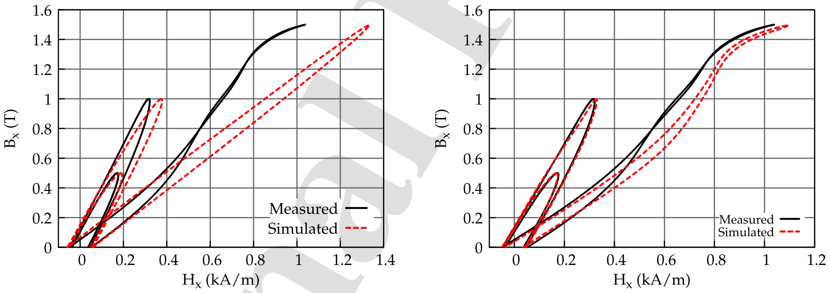

(e) IJAM (f) AJAM

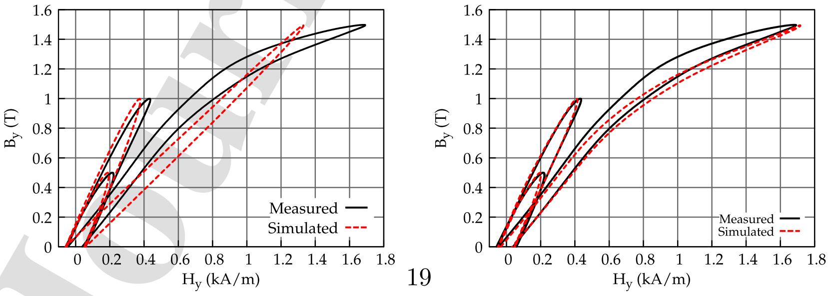

(g) IJAM (h) AJAM

Figure 9: Measured and FE simulated rotational field loci in the sensor region of the RRSST sample. (a), (c), (e), and (g) FEM coupled with the IJAM. (b), (d), (f), and (h) FEM coupled with the AJAM. (a) and (b) $H_x(H_y)$ loci. (c) and (d) $B_x(B_y)$ loci. Likewise, (e) and (g) $B_x(H_x)$ loci. (f) and (h) $B_y(H_y)$ loci.

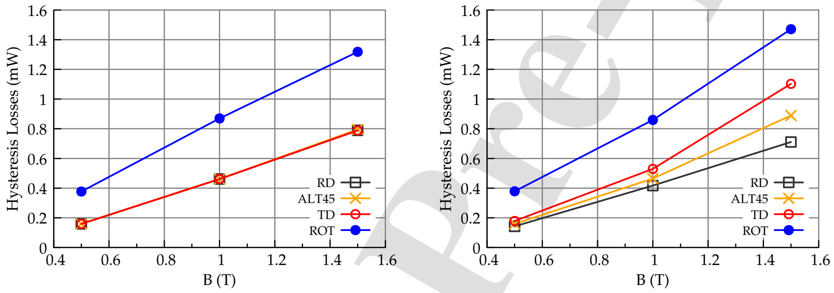

(a) IJAM (b) AJAM

Figure 10: FE simulated hysteresis losses in the RRSST sample for the cases when the magnetic flux density alternates in the RD, 45°, TD, and rotates in the counter clock-wise direction. (a) FEM coupled with the IJAM. (b) FEM coupled with the AJAM.

4. Conclusion

The anisotropic and isotropic JA models were included in the FEM. The FEA of the RRSST sample—circular steel sheet of grade M400-50A—was considered. The anisotropic JA model predicted the measured data better than the isotropic model. Moreover, the analysis proved that the anisotropic model is suitable for the FEA. Based on the computation time results, it seemed not to be very much more expensive than the isotropic model. The JA model's parameters depended on the flux density. An elliptical variation was assumed for the JA model's parameters.

Thus, it can be concluded that the anisotropic model is needed to model NO silicon steel laminations accurately. Moreover, using the proper anhysteretic magnetization and parameters improves the JA model's accuracy. The parameters of the improved JA model should be identified from several sets of measurement data and in different directions.

The parameters identified from the alternating measurements predict alternating fields that closely match the measured results. Additionally, they give reasonably good results for the rotational excitation at 0.5 T and 1 T. However, at 1.5 T, the predicted results differ significantly because the parameters are optimized for the alternating measurements. This may be considered as the limitation of the AJAM. Nevertheless, for an application such as an induction motor, the magnitude of the rotating magnetic field in the stator yoke is about 1 T, meaning the AJAM could be used to predict the field quantities.

References

[1] D. S. Petrovič, Non-oriented electrical steel sheets, Materials and Technology 44 (2010) 317–325.

[2] M. J. Sablik, D. C. Jiles, Coupled magnetoelastic theory of magnetic and magnetostrictive hysteresis, IEEE Trans. Magn. 29 (1993) 2113–2123.

[3] A. Raghunathan, Y. Melikhov, J. E. Snyder, D. C. Jiles, Modeling the temperature dependence of hysteresis based on Jiles-Atherton theory, IEEE Trans. Magn. 45 (2009) 3954–3957.

[4] L. Daniel, M. Rekik, O. Hubert, A multiscale model for magneto-elastic behaviour including hysteresis effects, Arch. Appl. Mech. 84 (2014) 1307–1323.

[5] C. Appino, C. Ragusa, F. Fiorillo, Can rotational magnetization be theoretically assessed?, Int. J. Appl. Electr. Mech. 44 (2014) 355–370.

[6] A. Kedous-Lebouc, S. Zouzou, P. Brisonneau, Anisotropy influence on the rotational and alternating field behavior of soft magnetic materials, IEEE Trans. Magn. 28 (1992) 2796–2798.

[7] S. Zurek, T. Meydan, Rotational power losses and vector loci under controlled high flux density and magnetic field in electrical steel sheets, IEEE Trans. Magn. 42 (2006) 2815–2817.

[8] K. Chwastek, Anisotropic properties of non-oriented steel sheets, IET-Electr. Power Appl. 7 (2013) 575–579.

[9] M. F. de Campos, Methods for texture improvement in electrical steels, Przeglad Elektrotechniczny 95 (2019) 7–11.

[10] F. Martin, D. Singh, A. Belahcen, P. Rasilo, A. Haavisto, A. Arkkio, Analytical model of magnetic anisotropy of non-oriented steel sheets, COMPEL-Int. J. Comput. Math Electr. Electron. Eng. 34 (2014) 1475–1488.

[11] F. Martin, D. Singh, P. Rasilo, A. Belahcen, A. Arkkio, Model of magnetic anisotropy of non-oriented steel sheets for finite-element method, IEEE Trans. Magn. 52 (2016) 1–4.

[12] S. Higuchi, T. Nakao, Y. Takahashi, T. Tokumasu, K. Fujiwara, Y. Ishihara, Modeling of two-dimensional magnetic properties based on one-dimensional magnetic measurements, IEEE Trans. Magn. 48 (2012) 3486–3489.

[13] S. Higuchi, Y. Takahashi, T. Tokumasu, K. Fujiwara, Comparison between modeling methods of 2-D magnetic properties in magnetic field analysis of synchronous machines, IEEE Trans. Magn. 50 (2014) 7009104.

[14] P. Handgruber, A. Stermecki, O. Bíró, V. Goričan, E. Dlala, G. Ofner, Anisotropic generalization of vector Preisach hysteresis models for nonoriented steels, IEEE Trans. Magn. 51 (2015) 1–4.

[15] J. V. Leite, N. Sadowski, P. Kuo-Peng, N. J. Batistela, J. P. A. Bastos, A. A. D. Espíndola, Inverse Jiles-Atherton vector hysteresis model, IEEE Trans. Magn. 40 (2004) 1769–1775.

[16] W. Li, I. H. Kim, S. M. Jang, C. S. Koh, Hysteresis modeling for electrical steel sheets using improved vector Jiles-Atherton hysteresis model, IEEE Trans. Magn. 47 (2011) 3821–3824.

[17] A. Bergqvist, A. Lundgren, G. Engdahl, Experimental testing of an anisotropic vector hysteresis model, IEEE Trans. Magn. 33 (1997) 4152–4154.

[18] S. Steentjes, F. Henrotte, K. Hameyer, Energy-based ferromagnetic material model with magnetic anisotropy, J. Magn. Magn. Mater. 425 (2017) 20–24.

[19] D. Lin, P. Zhou, A practical anisotropic vector hysteresis model based on play hysterons, IEEE Trans. Magn. 53 (2017) 7301206.

[20] T. Matsuo, M. Miyamoto, Dynamic and anisotropic vector hysteresis model based on isotropic vector play model for nonoriented silicon steel sheet, IEEE Trans. Magn. 48 (2012) 215–218.

[21] L. Daniel, O. Hubert, N. Buiron, R. Billardon, Reversible magneto-elastic behavior: A multiscale approach, J. Mech. Phys. Solids 56 (2008) 1018–1042.

[22] L. Bernard, L. Daniel, Effect of stress on magnetic hysteresis losses in a switched reluctance motor: Application to stator and rotor shrink fitting, IEEE Trans. Magn. 51 (2015) 1–13.

[23] H. Hauser, Y. Melikhov, D. C. Jiles, Examination of the equivalence of ferromagnetic hysteresis models describing the dependence of magnetization on magnetic field and stress, IEEE Trans. Magn. 45 (2009) 1940–1949.

[24] F. Henrotte, A. Nicolet, K. Hameyer, An energy-based vector hysteresis model for ferromagnetic materials, COMPEL-Int. J. Comput. Math Electr. Electron. Eng. 25 (2006) 71–80.

[25] B. Ducharne, S. Zurek, L. Daniel, G. Sebald, An anisotropic vector hysteresis model of ferromagnetic behavior under alternating and rotational magnetic field, J. Magn. Magn. Mater. 549 (2022) 169045.

[26] A. Krings, J. Soulard, Overview and comparison of iron loss models for electrical machines, J. Elec. Eng. 10 (2010) 162–169.

[27] J. Sievert, Two-dimensional magnetic measurements - history and achievements of the workshop, Przeglad Elektrotechniczny 87 (2011) 2–10.

[28] V. Goričan, A. Hamler, B. Hribernik, M. Jesenik, M. Trlep, Proceedings of 6th international workshop on 1&2-dimensional magnetic measurement and testing, Bad Gastein, Austria, 2000, pp. 66–75.

[29] V. Goričan, A. Hamler, M. Jesenik, B. Štumberger, M. Trlep, Measurement of magnetic properties of grain oriented silicon steel using round rotational single sheet tester (RRSST),

J. Magn. Magn. Mater. 320 (2003) 763–768.

[30] B. Upadhaya, P. Rasilo, L. Perkkiö, P. Handgruber, A. Benabou, A. Belahcen, A. Arkkio, Alternating and rotational loss prediction accuracy of vector Jiles-Atherton model, J. Magn. Magn. Mater. 527 (2021) 167690.

[31] B. Upadhaya, L. Perkkiö, P. Rasilo, A. Belahcen, P. Handgruber, A. Arkkio, Representation of anisotropic magnetic characteristic observed in a non-oriented silicon steel sheet, AIP Advances 10 (2020) 065222.

[32] A. Bergqvist, A simple vector generalization of the Jiles-Atherton model of hysteresis, IEEE Trans. Magn. 32 (1996) 4213–4215.

[33] D. Jiles, D. Atherton, Theory of ferromagnetic hysteresis, J. Magn. Magn. Mater. 61 (1986) 48–60.

[34] D. C. Jiles, J. B. Thoelke, M. K. Devine, Numerical determination of hysteresis parameters for the modelling of magnetic properties using the theory of ferromagnetic hysteresis, IEEE Trans. Magn. 28 (1992) 27–35.

[35] J. Gyselinck, P. Dular, N. Sadowski, J. Leite, J. P. A. Bastos, Incorporation of a Jiles-Atherton vector hysteresis model in 2D FE magnetic field computations: Application of the Newton-Raphson method, COMPEL-Int. J. Comput. Math Electr. Electron. Eng. 23 (2004) 685–693.

[36] J. H. Krah, A. J. Bergqvist, Numerical optimization of a hysteresis model, Physica B: Condens. Matter 343 (2004) 35–38.

[37] M. Galassi, et al., GNU scientific library reference manual, gsl-ref.pdf, 2019. URL: `https://www.gnu.org/software/gsl/doc/latex/gsl-ref.pdf`.

[38] J. P. A. Bastos, N. Sadowski, Electromagnetic Modeling by Finite Element Methods, CRC press, 2003.

[39] M. Chiampi, D. Chiarabaglio, M. Repetto, A Jiles-Atherton and fixed-point combined technique for time periodic magnetic field problems with hysteresis, IEEE Trans. Magn. 31 (1995) 4301–4311.

[40] E. Dlala, A. Belahcen, A. Arkkio, A fast fixed-point method for solving magnetic field problems in media of hysteresis, IEEE Trans. Magn. 44 (2007) 1214–1217.

[41] T. A. Davis, Direct methods for sparse linear systems, SIAM (2006).

[42] E. Dlala, A. Arkkio, Measurement and analysis of hysteresis torque in a high-speed induction machine, IET-Electr. Power Appl. 1 (2007) 737–742.

[43] C. Geuzaine, J. F. Remacle, Gmsh: a three-dimensional finite element mesh generator with built-in pre- and post-processing facilities, Int. J. Num. M. Eng. 79 (2009) 1309–1331.

[44] K. Atallah, D. Howe, Calculation of the rotational power loss in electrical steel laminations from measured H and B, IEEE Trans. Magn. 29 (1993) 3547–3549.

Highlights

1. Finite element level validation of an anisotropic Jiles-Atherton hysteresis model for NO FeSi electrical steel sheet.
2. Inclusion of the isotropic and anisotropic Jiles-Atherton hysteresis model in the 2D finite element method.
3. Finite element analysis of a round rotational single sheet tester.
4. Comparison of the finite element analysis results with the measurement data.
5. The anisotropic Jiles-Atherton hysteresis model predicts alternating and rotational field strength loci better than the isotropic Jiles-Atherton hysteresis model.

Author Statement

Brijesh Upadhaya: Conceptualization, Methodology, Formal Analysis, Writing- Original draft preparation. **Paavo Rasilo:** Reviewing. **Paul Handgruber:** Resources. **Anouar Belahcen**: Reviewing and Supervision. **Antero Arkkio:** Reviewing.

Potential competing interests do not exist.